PAPER

Accurate 3-Dimensional Imaging Method Based on Extended RPM for Rotating Target Model

Shouhei KIDERA[†a)], **Hiroyuki YAMADA**[††], ***and*** **Tetsuo KIRIMOTO**[†], ***Members***

SUMMARY Three-dimensional (3-D) reconstruction techniques employed by airborne radars are essential for object recognition in scenarios where optically vision is blurry, and are required for the monitoring of disasters and coast-guard patrols. There have been reports on 3-D reconstruction methods that exploit the layover appearing in inverse synthetic aperture radar (ISAR) imagery, which are suitable for the recognition of artificial targets such as buildings, aircraft or ships. However, existing methods assume only a point target or the aggregate of point targets, and most require the tracking of the multiple points over sequential ISAR images. In the case of a solid object with a continuous boundary, such as a wire or polyhedral structure, the positioning accuracy of such methods is severely degraded owing to scattering centers continuously shifting on the target surface with changes in the rotation angle. To overcome this difficulty, this paper extends the original Range Points Migration (RPM) method to the ISAR observation model, where a double mono-static model with two transmitting and receiving antennas is introduced to suppress cross-range ambiguity. The results of numerical simulation and experimental validation demonstrate that the extended RPM method has a distinct advantage for accurate 3-D imaging, even for non-point targets.

key words: *3-D image reconstruction, ISAR, target with continuous boundary, extended RPM, scattered center shifting*

1. Introduction

Microwave imaging systems are indispensable tools for geosurface measurement or target recognition even in optically harsh environments, such as in conditions of adverse weather or darkness. In particular, the surveillance radar for coast-guard security strongly requires an accurate 3-D target reconstruction method that can discriminate unidentified ships and refugee boats. As the existing approach to address this issue, the interferometric SAR (InSAR) based method outputs 3-D structures on geosurfaces [1], [2], but its is basically not suitable for objects with a discontinuous height distribution, such as buildings, aircraft or ships, owing to phase uncertainty.

To tackle this difficulty, some 3-D imaging methods based on layover appearing in ISAR imagery have been intensively developed [3], e.g., the method based on high resolution spectral estimation theory [4], the frequency stepping approach to compensate phase drift for accuracy enhancement [5] and introducing interferometry to 3-D inverse problems [6]–[8]. Among the recent studies [9], [10], 3-D geometry is more accurately obtained by exploiting multiple ISAR images, or so-called ISAR movies, where target points are sequentially tracked over multiple ISAR images. While these methods accomplish accurate target reconstruction for multiple point targets with sufficient separation greater the than range and azimuthal resolution, it is not appropriate for general solid targets, such as wire or polyhedral structures. This is because (1) each scattering center continuously shifts across the target's boundary with a change in rotation angle and (2) the approach requires the correct association of target points or image pairing over multiple ISAR images. Therefore, the above 3-D ISAR methods suffer accuracy degradation, particular for targets with continuous shape, like wires, rings, or objects with smooth surfaces. Such difficulties are fatal to all ISAR-based methods, since the multiple point target assumption is completely invalid in this case. Other approaches based on the circular InSAR [11], [12] have been developed for 3-D reconstruction for continuous boundary objects, which basically employ the interferometric approach for SAR obtained by the two circular scanning observations. However, these methods assume that target boundary is expressed as single-value function, and also require the image pairing between the multiple SAR images, which can generate the accuracy degradation for more complicated or discontinous surface represented by multiple-value function.

In contrast to the above approach, in recent years, high-resolution and highly accurate 3-D imaging methods for near-field ultra wideband (UWB) radar have been intensively developed after official approval of the commercial use of the UWB signal. In near-field measurement, the aforementioned problem that the scattering center shifts on a continuous target boundary becomes more severe. As a promising solution to this problem, SEABED [13], Envelope [14] and RPM [15], [16] have been proposed in the past decade as "not SAR-based" 3-D reconstruction methods. While SEABED accomplishes quite fast imaging based on the reversible transform between the range curves and the target boundary, it is applicable only to simply shaped objects owing to the use of range derivative, where the range curve should be accurately extracted and be correctly connected. On the contrary, RPM achieves accurate and fast imaging applicable to complex-shaped or multiple objects, and it directly and accurately estimates the direction of arrival (DOA) employing statistical properties for the range point distribution, and does not require a derivative opera-

Manuscript received February 28, 2012.
Manuscript revised June 22, 2012.

[†]The authors are with the Graduate School of Informatics and Engineering, The University of Electro-Communications, Chofu-shi, 182-8585 Japan.
[††]The authors is with Software Division, Hitachi Ltd., Yokohama-shi, 244-0817 Japan.
a) E-mail: kidera@ee.uec.ac.jp

DOI: 10.1587/transcom.E95.B.3279

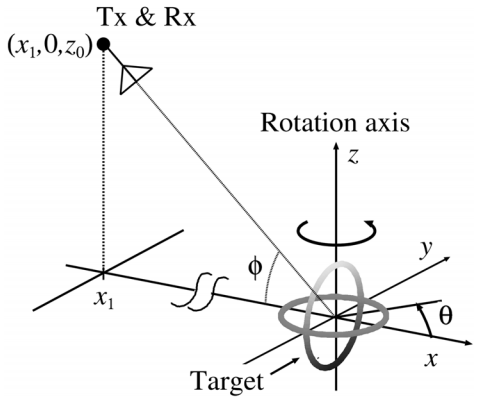

Fig. 1 System model assumed in the conventional ISAR based method.

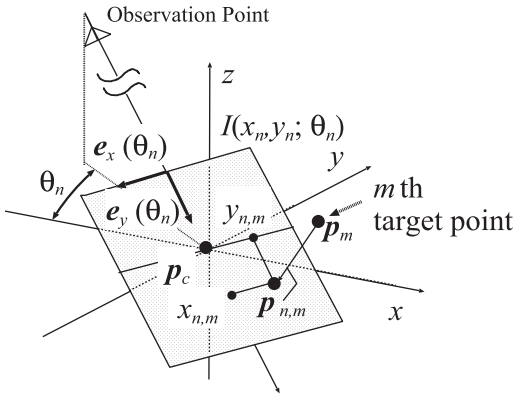

Fig. 2 Spatial relationship between ISAR imaging plane and pointwise target.

tion or range point connection.

With this background, the present paper newly introduces a 3-D imaging method by extending the original RPM method [15] to a rotating target model; i.e., an ISAR model. The notable advantage of RPM is that it is applicable to an arbitrary scanning orbit, and is readily extended to the ISAR model. In addition, this study employs a double mono-static model, in which two transmitting and receiving antennas are assumed, to suppress cross-range ambiguity in the 3-D imaging. Furthermore, the extended RPM divides the range points into two groups, which are employed to enhance the accuracy and resolution along two orthogonal directions on the cross-range plane. The results obtained from numerical simulation and experimental data, based on a 1/100 downscale model of X-band radar system except for the center frequency, show that our proposed method accomplishes fast and accurate 3-D reconstruction of a target, even for targets with continuous boundaries.

2. Observation Model

Figure 1 shows the observation model. It assumes that a mono-static radar with a set of transmitting and receiving antenna is located at $(x_1, 0, z_0)$. It also assumes that a target has an arbitrary shape (e.g. point-wise or a general solid object with a continuous boundary) and exists around the origin, for simplicity. The target rotates with uniform angular velocity about the z axis, and its motion is completely given. The glazing angle is defined as ϕ. In each rotation angle θ, the antenna receives the complex-valued reflection signal $s(\theta, f)$ for each frequency f, which is swept in the finite frequency range. Without loss of generality, this paper assumes the equivalent observation model that an antenna scans along the circumference of circle with radius x_1 and center $(0, 0, z_0)$ around a static object.

3. Conventional Method

3.1 3-D Reconstruction Scheme Based on Multiple ISAR Images

Various 3-D reconstruction techniques, based on ISAR images, have been proposed and their effectiveness has been verified for some typical cases [3]–[8]. In particular, for high-resolution 3-D imaging based on range-Doppler azimuthal compression, a method [9] or [10] employing layover in ISAR imagery has been already proposed, where the focused target points are tracked over multiple ISAR frames. This section briefly explains the 3-D reconstruction process for this method detailed in [9], and states the problem exemplified by typical target cases.

Here, $I(x_n, y_n; \theta_n)$ is defined as the ISAR image obtained for the observation angle θ_n, $(n = 1, \cdots, N)$. These sequential images can be obtained with low computation cost by using polar format algorithm (PFA) [17], which is based on the two-dimensional (2-D) Fourier transform converting from the spatial spectra of phase-compensated received signals to the ISAR images by polar coordinate interpolation. The significant focused points extracted from local maxima of $I(x_n, y_n; \theta_n)$ are denoted $\boldsymbol{p}_{n,m} = (x_{n,m}, y_{n,m})$, where m is the index number of the target points. Figure 2 shows the spatial relationship between the image plane and the m-th target point as $\boldsymbol{p}_m$ at the observation angle θ_n. This method is then used to estimate the target point as $\tilde{\boldsymbol{p}}_{n+1,m}$ in the next ISAR image at θ_{n+1} on basis of the nearest-neighbor scheme:

$$\tilde{\boldsymbol{p}}_{n+1,m} = \arg\min_{\boldsymbol{p}_{n+1,m'}} \|\boldsymbol{p}_{n+1,m'} - \boldsymbol{p}_c - \boldsymbol{R}(\Delta\theta)(\boldsymbol{p}_{n,m} - \boldsymbol{p}_c)\|, \quad (1)$$

where, $\boldsymbol{R}(*)$ denotes the rotation matrix, $\boldsymbol{p}_c$ is the location of the center of the assumed imaging plane $I(x_n, y_n; \theta_n)$, which is set to the origin in this case, and $\Delta\theta = \theta_{n+1} - \theta_n$ is the interval of the rotation angle. If the evaluation value defined in the right term of Eq. (1) exceeds a set threshold, this point is eliminated as a candidate for the false image resulting from random errors or other components.

Finally, the 3-D coordinates of a target point as $\boldsymbol{p}_m$ are obtained taking the least-squared-errors approach weighted with the image intensity:

$$\hat{\boldsymbol{p}}_m = (\boldsymbol{A}^T \boldsymbol{W} \boldsymbol{A})^{-1} \boldsymbol{A}^T \boldsymbol{W} \boldsymbol{b}_m + \boldsymbol{p}_c, \quad (2)$$

where $\boldsymbol{W}$, $\boldsymbol{A}$ and $\boldsymbol{b}_m$ are defined as

$$\boldsymbol{W} = \mathrm{diag}\Big[I(\boldsymbol{p}_{n,m};\theta_n), I(\tilde{\boldsymbol{p}}_{n+1,m};\theta_n), \cdots, I(\tilde{\boldsymbol{p}}_{n+L,m};\theta_{n+L}), I(\boldsymbol{p}_{n,m};\theta_n), I(\tilde{\boldsymbol{p}}_{n+1,m};\theta_n), \cdots, I(\tilde{\boldsymbol{p}}_{n+L,m};\theta_{n+L})\Big], \quad (3)$$

$$\boldsymbol{A} = \Big[\boldsymbol{e}_x(\theta_n), \cdots, \boldsymbol{e}_x(\theta_{n+L}), \boldsymbol{e}_y(\theta_n), \cdots, \boldsymbol{e}_y(\theta_{n+L})\Big]^T, \quad (4)$$

$$\boldsymbol{b}_m = [x_{n,m}, \tilde{x}_{n+1,m}, \cdots, \tilde{x}_{n+L,m}, y_{n,m}, \tilde{y}_{n+1,m}, \cdots, \tilde{y}_{n+L,m}]^T. \quad (5)$$

L is the number of ISAR images used for 3-D reconstruction, $(\tilde{x}_{n,m+i}, \tilde{y}_{n,m+i}) = \tilde{\boldsymbol{p}}_{n,m+i}$, $(i = 1, \cdots, L)$, $\boldsymbol{e}_x(\theta_n)$ denotes a 3-D unit vector directed from the observation point to $\boldsymbol{p}_c$, and $\boldsymbol{e}_y(\theta_n)$ is a unit vector orthogonal to $\boldsymbol{e}_x(\theta_n)$ on the imaging plane $I(x_n, y_n; \theta_n)$ as shown in Fig. 2.

3.2 Numerical Examples and Statement of Problem

Reconstruction examples employing the above method are numerically investigated to discuss its imaging property. For simplicity, regardless of whether a target has multiple target points or has a continuous boundary, the scattered electric field for each rotation angle θ_n is calculated using the Born approximation, i.e., the multiple scattering effect is not considered,

$$S(\theta_n, f) = \begin{cases} \sum_{m=1}^{M_T} \frac{A_m}{R_m(\theta_n)} \mathrm{e}^{-\mathrm{j}\frac{4\pi f R_m(\theta_n)}{\mathrm{c}}}, & (f_{\min} \le f \le f_{\max}), \\ 0, & (\text{Otherwise}), \end{cases} \quad (6)$$

where M_T is the total number of the point scatterers, c is the propagation speed in air, and $R_m(\theta_n)$ denotes the distance between the antenna and the m-th point scatterer for an observation angle θ_n. A_m is the reflection amplitude for each scatterer and is constant in this case. $(x_1, 0, z_0) = (-150\cos\phi\Delta R, 0.0\Delta R, 150\sin\phi\Delta R)$, where ΔR denotes a slant range resolution, and $\phi = \pi/6$ holds. This simulation assumes a typical X-band observation model, where the slant range resolution is around 1 m and the center frequency is around 10 GHz. To adjust the possible experimental setup described in the following section, a 1/100 downscaled model for geometry and range resolution is adopted. However, with regard to the center frequency of the transmitted signal, it is difficult to adjust it to a realistic value (THz frequency required in 1/100 model) because of the limitation of the experimental device, and a 1/3 downscale model was then used. Namely, the minimum and maximum frequencies $f_{\min}$ and $f_{\max}$ used in creating the received signal are 24 and 40 GHz, respectively. The central wavelength λ is 9.375 mm and the nominal slant-range resolution ΔR is also 9.375 mm. The total number of observation samples is 3601 for $0 \le \theta_n \le 2\pi$, to ensure sufficient interpolation accuracy for the PFA algorithm. Figures 3 and 4 illustrate the ISAR images with $\theta_n = 0$ and $\theta_n = \pi/9$, and the 3-D image obtained using the conventional method, where 8 point targets are located on the vertices of a cuboid, having a width of $10\Delta R$, depth of $14\Delta R$, height of $10\Delta R$, and its center being set to the origin. Figure 3 shows that the projected target

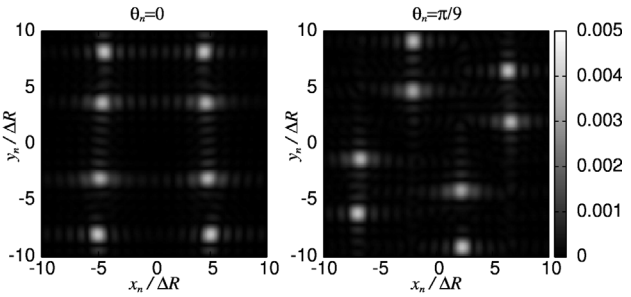

Fig. 3 ISAR images for multiple point targets at the rotation angles $\theta = 0$ (left) and $\theta = \pi/9$ (right).

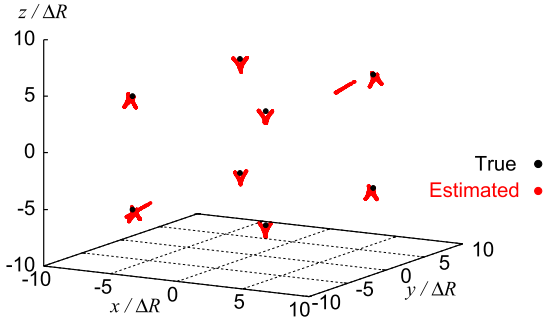

Fig. 4 3-D reconstruction image for multiple point targets by the conventional method.

points are sufficiently separated on the obtained ISAR images, and consequently, Fig. 4 demonstrates that the conventional method accurately reconstructs 3-D positions of the multiple target points, and that the tracking scheme is successful. By contrast, Figs. 5 and 6 present the same views as in Figs. 3 and 4, but for the two annular objects orthogonally criss-crossed as in Fig. 1. Each annular target has a radius of $10\Delta R$, and its center is set to the origin. This example raises the serious problem that the 3-D image obtained using the conventional method severely suffers from the inaccuracy, and cannot reconstruct the annular target existing on $z = 0$ plane at all. This problem mainly arises because the scattering center moves across the target boundary as a target with a continuous boundary rotates. The approach of tracking points in ISAR images is then invalid, and the imaging accuracy deteriorates drastically. Figure 7 illustrates the example of the dominant scattering center shifting for different observation angles. As shown in this figure, the scattering centers, observed at different observation angles, continuously move across the target's boundary or surface and are difficult to track.

4. Extended RPM Method

As a solution to the aforementioned problem, this paper extends the original RPM method [15], which has realized accurate and fast 3-D imaging for static objects. A notable advantage of this method is that it is basically applicable to an arbitrary scanning trajectory and, thus naturally to the ISAR observation model, because the rotation of the target

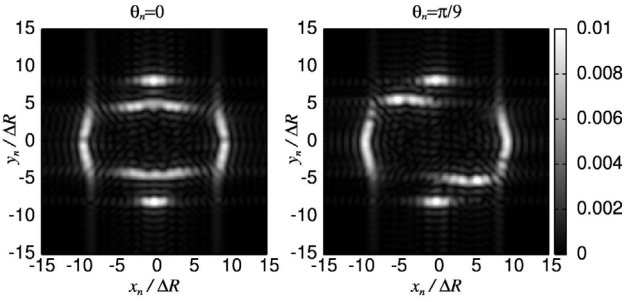

Fig. 5 ISAR images for two annular targets at the rotation angles $\theta = 0$ (left) and $\theta = \pi/9$ (right).

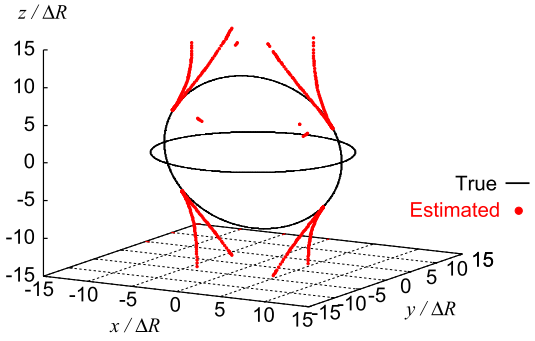

Fig. 6 3-D reconstruction image for two annular targets by the conventional method.

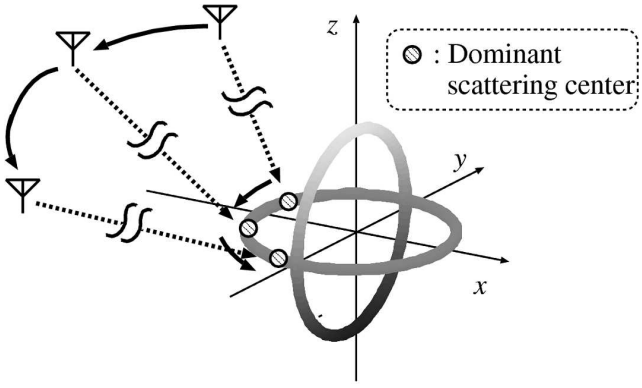

Fig. 7 Examples for dominant scattering center shifting for different observation angles.

is equivalent to the circular scanning of an antenna for a static object.

First of all, to avoid a reconstruction ambiguity along the cross-range direction, the extended RPM method employs double mono-static observation models as shown in Fig. 8. The cross-range ambiguity appearing in a single mono-static model is essentially inevitable in RPM imaging, because this method basically employs spatial-domain interferometry for 3-D reconstruction. Figure 9 presents the diagrams showing the cross range ambiguity for single and double mono-static models and shows that the cross-range ambiguity is eliminated applying spatial interferometry for antennas #1 and #2. This system can be implemented for

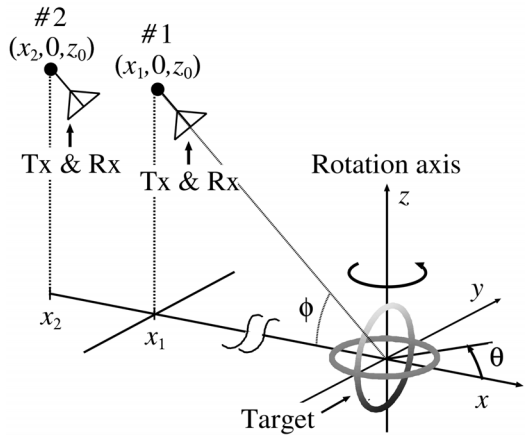

Fig. 8 Double mono-static model used in the extended RPM method.

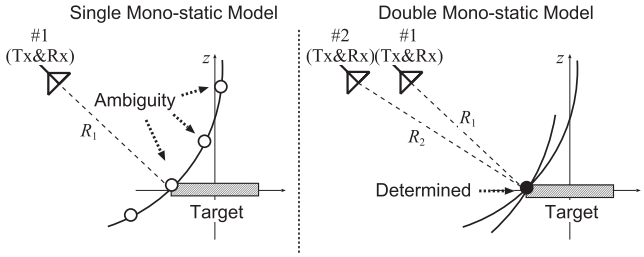

Fig. 9 Ambiguity appearing along cross-range direction in single mono-static (left) and eliminated in the double mono-static models (right).

radar mounted on a helicopter or airplane, where #1 and #2 antennas are set to the head and tail of them, respectively.

4.1 Extended RPM for Target Rotating Model

This method assumes that the previous double mono-static model can be regarded as that a set of transmitting and receiving antennas scan along the circumstances of two circles whose centers are $(0, 0, z_0)$ and radii are x_1 and x_2. In this model, each antenna location is redefined as $(X, Y, z_0) = (x_k \cos\theta_n, x_k \sin\theta_n, z_0), (k = 1, 2)$. At each antenna location, the significant range R is extracted from the local maximum of the received signal as $S(X, Y, R)$, which is obtained applying the Capon method to $s(\theta_n, f)$ [16], the processing is detailed in the next subsection. The group $\boldsymbol{q}_i = (X_i, Y_i, R_i)$, $(i = 1, \cdots, N_{\mathrm{Q}})$ called "range points", is then obtained at both #1 and #2 antennas, where N_{Q} denotes the total number of range points. This method basically assumes that the target boundary point corresponding to $\boldsymbol{q}_i$ exists on the sphere with center (X_i, Y_i, z_0) and radius R_i. The extended RPM determines the location of the scattering point on the target for each $\boldsymbol{q}_i$ by exploiting the spatial distribution of the intersection points among the spheres with neighboring range points:

$$\hat{\boldsymbol{p}}(\boldsymbol{q}_i) = \underset{\boldsymbol{p}^{\mathrm{int}}(\boldsymbol{q}_i;\boldsymbol{q}_j,\boldsymbol{q}_k)\in\mathcal{P}_i}{\arg\max} \sum_{l=1}^{N_{\mathrm{M}}} \sum_{m=1}^{N_{\mathrm{S}}} f(\boldsymbol{p}^{\mathrm{int}}(\boldsymbol{q}_i; \boldsymbol{q}_j, \boldsymbol{q}_k))$$

$$\times \exp\left\{-\frac{\|\boldsymbol{p}^{\mathrm{int}}(\boldsymbol{q}_i;\boldsymbol{q}_j,\boldsymbol{q}_k)-\boldsymbol{p}^{\mathrm{int}}(\boldsymbol{q}_i;\boldsymbol{q}_l,\boldsymbol{q}_m)\|^2}{2\sigma_r^2}\right\}, \tag{7}$$

where $\boldsymbol{p}^{\mathrm{int}}(\boldsymbol{q}_i;\boldsymbol{q}_j,\boldsymbol{q}_k)$ denotes the intersection point among the three spheres, determined by the range points $\boldsymbol{q}_i$, $\boldsymbol{q}_j$ and $\boldsymbol{q}_k$, and σ_r is an empirically determined constant. The evaluation function $f(\boldsymbol{p}^{\mathrm{int}}(\boldsymbol{q}_i;\boldsymbol{q}_j,\boldsymbol{q}_k))$ is defined as

$$f(\boldsymbol{p}^{\mathrm{int}}(\boldsymbol{q}_i;\boldsymbol{q}_j,\boldsymbol{q}_k)) = S(\boldsymbol{q}_j)\exp\left\{-\frac{D(\boldsymbol{q}_i,\boldsymbol{q}_j)^2}{2\sigma_X^2}\right\} + S(\boldsymbol{q}_k)\exp\left\{-\frac{D(\boldsymbol{q}_i,\boldsymbol{q}_k)^2}{2\sigma_X^2}\right\} \tag{8}$$

where $S(\boldsymbol{q}_j)$ denotes the output amplitude of the Capon algorithm, $D(\boldsymbol{q}_i,\boldsymbol{q}_j) = \sqrt{(X_i-X_j)^2+(Y_i-Y_j)^2}$, and σ_X is an empirically determined constant. Here, this method divides the range points into two groups to accurately calculate the intersection points $\boldsymbol{p}^{\mathrm{int}}(\boldsymbol{q}_i;\boldsymbol{q}_j,\boldsymbol{q}_k)$, which is an advanced point in the extended RPM algorithm. Thus, $\mathcal{P}_i$ is defined as

$$\mathcal{P}_i = \left\{\boldsymbol{p}^{\mathrm{int}}(\boldsymbol{q}_i;\boldsymbol{q}_j,\boldsymbol{q}_k)\middle|\boldsymbol{q}_j\in Q_i^{\mathrm{M}},\boldsymbol{q}_k\in Q_i^{\mathrm{S}}\right\}, \tag{9}$$

where Q_i^{M} expresses a set of range points, where $\sqrt{X_i^2+Y_i^2} = \sqrt{X_j^2+Y_j^2}$ is satisfied, i.e., the group of the antennas on the same scanning radius for $\boldsymbol{q}_i$. Otherwise, Q_i^{S} expresses a set of range points, where $\sqrt{X_i^2+Y_i^2} \neq \sqrt{X_k^2+Y_k^2}$ is satisfied, i.e., the group of the antennas on the different scanning radius for $\boldsymbol{q}_i$. Then, N_{M} and N_{S} are the numbers of the range points included in Q_i^{M} and Q_i^{S}, respectively. Figure 10 illustrates an example of Q_i^M and Q_i^{S} in the two cases as $\sqrt{X_i^2+Y_i^2} = x_1$ and $\sqrt{X_i^2+Y_i^2} = x_2$, respectively. Figure 11 presents the spatial relationship between the intersection points and the target boundary. As shown in this figure, the two intersection lines L_i^{M} and L_i^{S}, which is determined by range points in Q_i^M and Q_i^{S}, becomes nearly orthogonal, which enhances the positioning accuracy of the intersection point on the cross-range plane. This method determines each scattering center observed from different angles, and is thus applicable to general solid objects with continuous boundaries avoiding the local connection of range points.

4.2 Range Extraction Employing Capon Algorithm

As the preprocessing of the extended RPM method, we briefly explain the procedure for extracting range points based on the Capon method [16]. Here, $s(X,Y,f)$ is defined as the received signal observed at $(X,Y,z_0) = (x_k\cos\theta, x_k\sin\theta), (k=1,2)$. First, $\boldsymbol{V}_n(X,Y)$ is defined as,

$$\boldsymbol{V}_n(X,Y) = \left[\frac{s(X,Y,f_n)}{s_{\mathrm{tr}}(f_n)},\cdots,\frac{s(X,Y,f_{n+M-1})}{s_{\mathrm{tr}}(f_{n+M-1})}\right]^T, \tag{10}$$

where $s_{\mathrm{tr}}(f)$ is the form of the frequency domain of the transmitted signal. M denotes the dimension of $\boldsymbol{V}_n(X,Y)$.

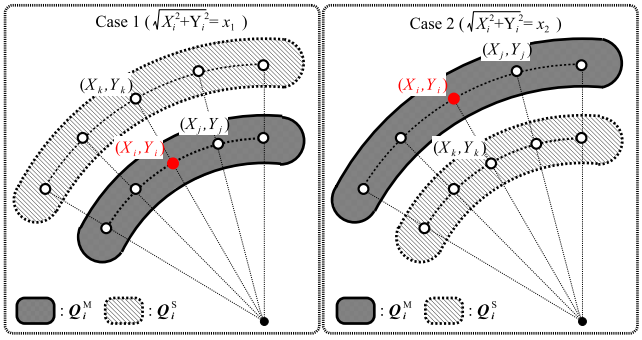

Fig. 10 Q_i^{M} and Q_i^{S} in the case that $\sqrt{X_i^2+Y_i^2} = x_1$ (left) and $\sqrt{X_i^2+Y_i^2} = x_2$ (right).

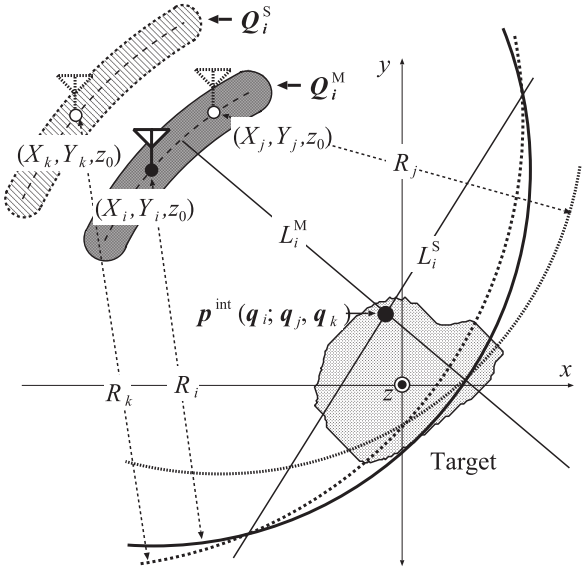

Fig. 11 Relationship among intersection point $\boldsymbol{p}^{\mathrm{int}}(\boldsymbol{q}_i;\boldsymbol{q}_j,\boldsymbol{q}_k)$, two intersection lines L_i^{M} and L_i^{S} and target boundary.

Frequency averaging is employed to suppress a range sidelobe caused by coherent interference signals, and the correlation matrix $\boldsymbol{C}(X,Y)$ is calculated as,

$$\boldsymbol{C}(X,Y) = \sum_{n=1}^{N-M+1}\boldsymbol{V}_n(X,Y)\boldsymbol{V}_n^H(X,Y), \tag{11}$$

where ^{H} denotes the Hermitian transpose. N is the total number of the frequency points, and is determined from the maximum frequency band of the transmitted signal. $M \le N$ holds. The output of the Capon algorithm $S(X,Y,R)$ is

$$S(X,Y,R) = \frac{1}{\boldsymbol{a}^H(R)\boldsymbol{C}(X,Y)^{-1}\boldsymbol{a}(R)}, \tag{12}$$

where $\boldsymbol{a}(R)$ denotes the steering vector of R for each frequency

$$\boldsymbol{a}(R) = \left[\mathrm{e}^{-\mathrm{j}4\pi f_n R/\mathrm{c}}, \mathrm{e}^{-\mathrm{j}4\pi f_{n+1} R/\mathrm{c}}, ..., \mathrm{e}^{-\mathrm{j}4\pi f_{n+M-1} R/\mathrm{c}}\right]^T. \tag{13}$$

4.3 Procedure of the Extended RPM Method

The procedure of the proposed method is summarized as follows.

Step 1). Outputs of the Capon algorithm as $S(X, Y, R)$ for received signals $s(X, Y, f)$ are obtained for each antenna location at (X, Y, z_0).

Step 2). Range points are extracted for each antenna location, satisfying

$$\left.\begin{array}{ll} \partial S(X,Y,R)/\partial R = & 0, \\ S(X,Y,R) & \geq \alpha \max\limits_{(X,Y,R)} s(X,Y,R), \end{array}\right\}. \tag{14}$$

where α is determined empirically, and the group of $\boldsymbol{q}_i = (X_i, Y_i, R_i)$, $(i = 1, \cdots, N_{\mathrm{Q}})$ are obtained.

Step 3). As for $\boldsymbol{q}_i$, the main set and sub set of the range points Q_i^{M} and Q_i^{S} are extracted, and the set of the intersection points as $\mathcal{P}_i$ is created using Eq. (9). Then, the optimum target point $\hat{\boldsymbol{p}}(\boldsymbol{q}_i)$ is calculated from Eq. (7).

Step 4). Step 3) is carried out for all range points and the set of target points as $\mathcal{T}_{\mathrm{rpm}} = \{\hat{\boldsymbol{p}}(\boldsymbol{q}_i) | i = 1, \cdots, N_{\mathrm{Q}}\}$ is obtained.

Step 5). False target points are removed from $\mathcal{T}_{\mathrm{rpm}}$ satisfying

$$\zeta\left(\hat{\boldsymbol{p}}(\boldsymbol{q}_i)\right) \leq \beta \max_i \zeta\left(\hat{\boldsymbol{p}}(\boldsymbol{q}_i)\right), \tag{15}$$

where β is empirically determined, and $\zeta(*)$ denotes the maximum evaluation value formulated as in the right term in Eq. (7).

5. Performance Evaluation

5.1 Numerical Simulation

This section presents numerical examples for the extended RPM method. First, the example in an ideal case, where the true range points (X, Y, R) are given, is investigated to clarify the accuracy limit of the proposed method. Figure 12 shows the 3-D image obtained using the extended RPM method, where the target is that in Fig. 6. $(x_1, 0, z_0) = (-150\cos\phi\Delta R, 0.0\Delta R, 150\sin\phi\Delta R)$ and $(x_2, 0, z_0) = (-150\cos\phi\Delta R - 25.0\Delta R, 0.0\Delta R, 150\sin\phi\Delta R)$ are set, where $\phi = \pi/6$ holds. In an actual case, the interval between the two antennas should be held around 25 m, which can be arrayed on the head and tail of a large helicopter or an aircraft. In addition, this interval should be set as large as possible, because, in the proposed method, it directly affects the imaging accuracy along the cross-range direction. $\sigma_r = 0.5\Delta R$ and $\sigma_X = 20.0\Delta R$ are set in this case. Figure 12 confirms that the extended RPM method produces an extremely accurate target 3-D image, even for objects with a continuous boundary. This result guarantees a distinct potential for 3-D reconstruction (i.e., the error of the imaging process in RPM is mostly negligible in itself in such an ideal case), which is a substantial advantage over the conventional ISAR-based methods. On the contrary, Figs. 13 and 14 present the extracted range points (X, Y, Z) at each antenna location, and the 3-D image obtained by the extended RPM method for the same target, respectively, where the received signals are calculated using Eq. (6), and the range points are extracted from the output of the Capon method described in Sect. 4.2. $\alpha = 0.2$ and $\beta = 0.3$ are set in this case. A noiseless situation is assumed. This figure also demonstrates that the extended RPM method achieves accurate 3-D imaging owing to the RPM advantage (i.e., accurate conversion from the range points to the target points without target point tracking). Here, the accuracy of the image mildly degrades compared with that in the ideal case shown in Fig. 12, particularly in the intersection area of two annulars, owing to the range point inaccuracy resulting from the interference effects as shown in the enlarged part of Fig. 13. However, this method accurately reconstructs the whole part of the target, even with continuous boundaries. To verify the flexibility of the extended RPM method, an example of multiple points target is considered, where the conventional method can offer an accurate 3-D image as in Fig. 4. In addition, since the interval of double mono-static radar can effect the reconstruction accuracy especially for the cross-range direction, this interval should be set as large as possible. Fig. 15 shows the 3-D reconstruction image for the multiple points object, where the same data as in Fig. 4 are used. The figure also validates the accurate 3-D imaging of the extended RPM method for such pointwise targets.

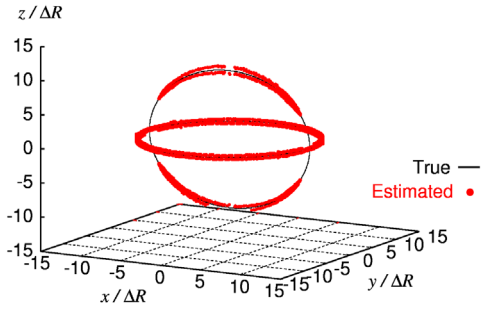

Fig. 12 3-D reconstruction image for two annular targets by the extended RPM method, where the true range points are given.

Furthermore, a noisy situation is investigated, whereby white Gaussian noise is added to each received signal $s(f, \theta)$. Figures 16 and 17 show the 3-D images obtained using the extended RPM method, in the cases of S/N = 20 and 10 dB, respectively. Here, S/N is defined as the ratio of the average signal power to that of noise in the frequency domain. These examples in noisy cases can verify the robust imaging property of the extended RPM method, in that the accuracy in each S/N case is not seriously degraded because the method exploits a statistical characteristic of the range points instead of locally connecting them.

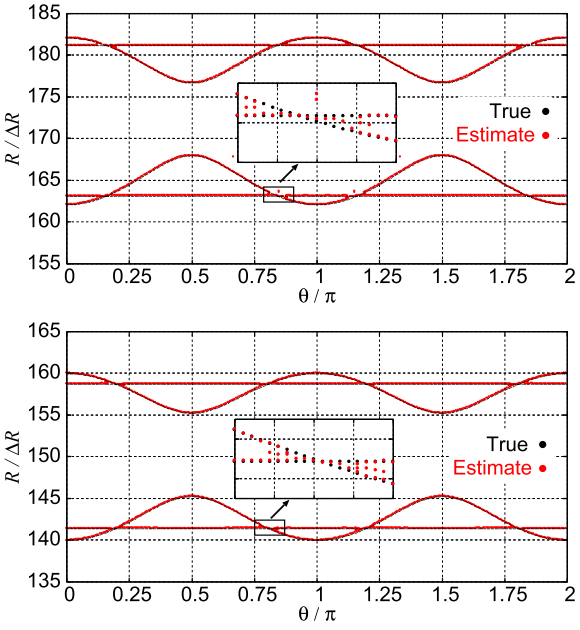

Fig. 13 Extracted range points extracted from the output of Capon method at x_1 (lower) and x_2 (upper).

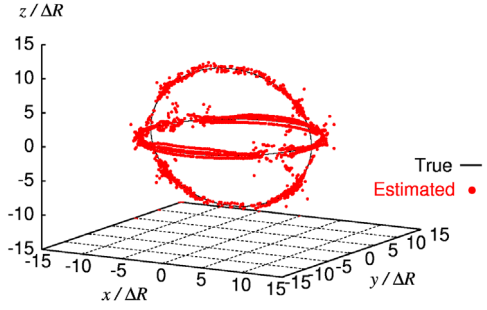

Fig. 14 3-D reconstruction image for two annular targets by the extended RPM method in noiseless case, where the range points are not given.

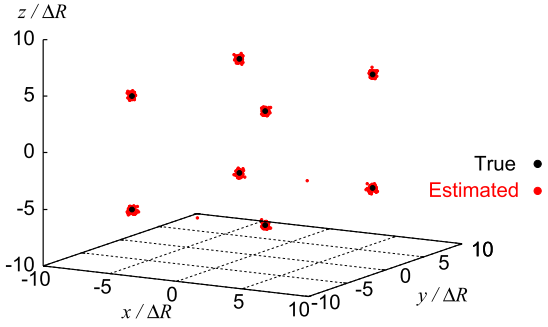

Fig. 15 3-D reconstruction image for multiple point targets by the extended RPM method in noiseless case, where the range points are not given.

Finally, the quantitative analysis for the 3-D image is introduced using ϵ_i defined as

$$\epsilon_i = \min_{\boldsymbol{p}_{\text{true}}} \|\boldsymbol{p}_{\text{true}} - \boldsymbol{p}_{\text{e}}^i\|, \quad (i = 1, 2, ..., N_{\text{T}}), \tag{16}$$

where $\boldsymbol{p}_{\text{true}}$ and $\boldsymbol{p}_{\text{e}}^i$ express the 3-D locations of the true and

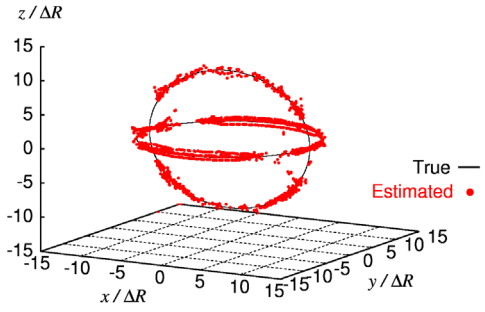

Fig. 16 3-D reconstruction image for two annular targets by the extended RPM method at S/N = 20 dB.

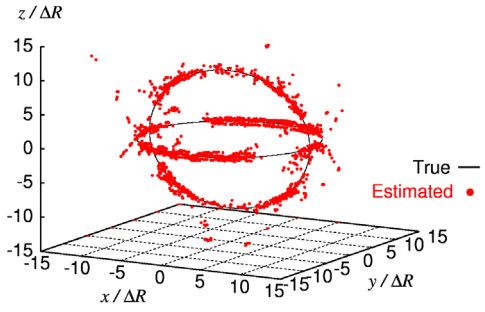

Fig. 17 3-D reconstruction image for two annular targets by the extended RPM method at S/N = 10 dB.

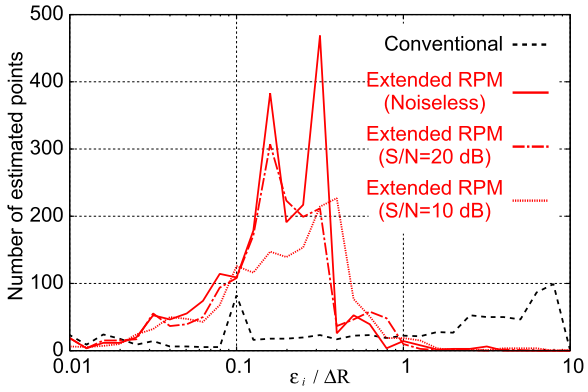

Fig. 18 Histogram of estimated target points for each error ϵ_i at two annular targets.

estimated target points, respectively. This value can measure the spatial errors for the reconstructed 3-D image by assessing the minimum distance to the actual target boundary point. N_{T} is the total number of $\boldsymbol{p}_{\text{e}}^i$. Figure 18 plots the number of estimated points for each value of ϵ in the cases of Figs. 6, 14, 16, and 17. It is verified that the number of accurate target points achieved with the extended RPM method significantly increases around $0.2\Delta R$, simultaneously enhancing the imaging range, while the conventional method produces many estimated points far from the actual boundaries. The mean value of ϵ_i as $\overline{\epsilon}$ is $2.37\Delta R$ for the conventional method. $\overline{\epsilon}$ for the proposed method is $0.20\Delta R$, $0.20\Delta R$ and $0.47\Delta R$ in noiseless, S/N=20 dB and S/N=10 dB cases, respectively. The accuracy of the pro-

posed method is basically determined by the S/N, when the targeted dominant scattering point is separated from the other points by greater than the slant range resolution. This result quantitatively demonstrates the robustness of the extended RPM method for accurate 3-D imaging in noisy situations. As reference, we assume that the accurate 3-D imaging is accomplished under the condition that the number of the target points with $\epsilon \leq 0.5\Delta R$ covers 90% of the total number of estimated points. In this case, this condition is achieved using the proposed method if S/N $\geq$ 20 dB. Note that, the center frequency in an actual scenario should be set to a higher value, where the waveform of the received signal would be different from that assumed in this model because of the frequency dependency of the scattering phenomenon [14]. While this waveform disparity can affect the performance of the proposed method, we consider that this effect can be negligible because our method employs only the range points and not the scattered waveform in the imaging process.

5.2 Experimental Study

This section presents the validation of each method using experimental data to assess the applicability for realistic situations. Figures 19 and 20 are a diagram of experimental setup and an illustration of the experimental scene, respectively. The same scaledown model assumed in numerical simulation is employed. The transmitting and receiving antennas are two horn antennas with 3 dB beam widths of 27 degrees, and separation of 48 mm. On the transmitter side, a 20 dB amplifier is inserted to obtain a sufficient echo from the targets. The received data for each frequency are acquired by a vector network analyzer (VNA), and the minimum and maximum frequencies are 24 and 40 GHz, respectively, where the slant-range resolution ΔR is 9.375 mm, and the central wavelength λ is 9.375 mm. The center locations of the transmitting and receiving antennas are set at $(x_1, 0, z_0) = (-141.1\Delta R, 0.0\Delta R, 79.1\Delta R)$ and $(x_2, 0, z_0) = (-168.3\Delta R, 0.0\Delta R, 79.1\Delta R)$, where the target is set at two different locations in the first and second observations to obtain the observation data for the double mono-static model. The two annular targets made of copper, located on the $x = 0$ and $z = 0$ planes, are orthogonally crisscrossed, and have diameters of $21.3\Delta R$ (200 mm), where its manufacturing precision is within 1 mm and is called "Case A". The actual spatial locations of the target and the antennas are measured by the laser range finder. The scattered signals from the targets are obtained by eliminating the direct signal from the transmitting antenna to the receiving antenna.

First, the example of the conventional ISAR based method is presented, where the observation data obtained at $(x_1, 0, z_0)$ are used. Figure 21 shows the ISAR images for the observation angles of $\theta_n = 0$ and $\theta_n = \pi/9$, respectively. The mean S/N is around 26 dB in this case. While there are some focal areas on the ISAR images, it is difficult to connect the these points over the neighboring images, owing to the scattering center shifting as described in the previous numerical examples. The 3-D reconstruction image in Fig. 22 thus cannot offer even the outline of the target boundary, and the accuracy is significantly degraded owing to the difficulty of tracking the focal image points.

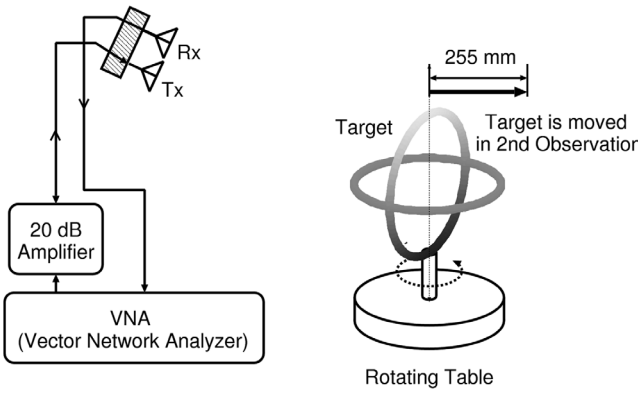

Fig. 19 Diagrams of experimental setup.

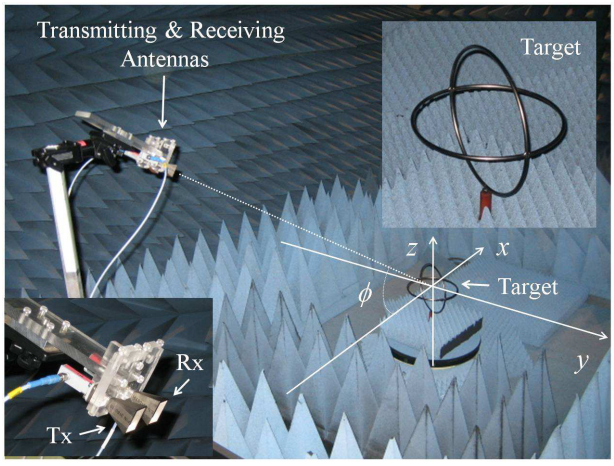

Fig. 20 Experimental equipment and its scene.

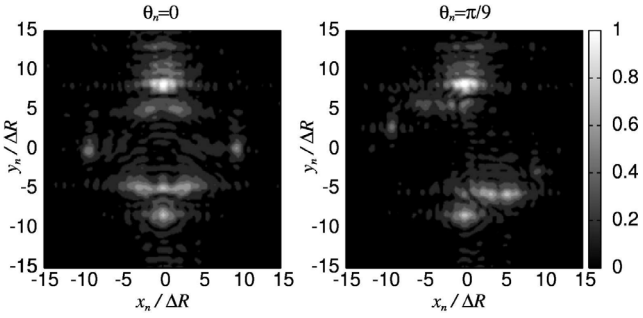

Fig. 21 ISAR images at the rotation angles $\theta = 0$ (left) and $\theta = \pi/9$ (right) in the experiment (Case A).

Next, the example of the extended RPM method is presented as follows. Figures 23 and 24 present the outputs of the Capon algorithm as $s(X, Y, R)$ and the extracted range points for each antenna at $(x_1, 0, z_0)$ and $(x_2, 0, z_0)$, respectively, where the same target as in Fig. 22 is assumed. The figures confirm that while there are distinguishable echoes

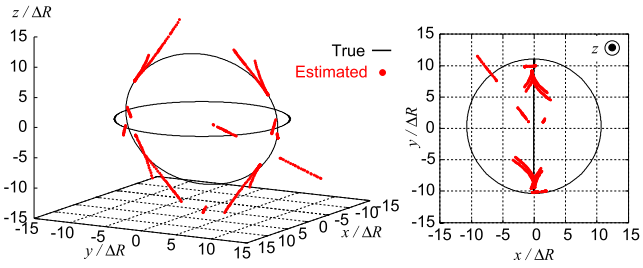

Fig. 22 3-D reconstruction image obtained by the conventional method in the experiment (Case A).

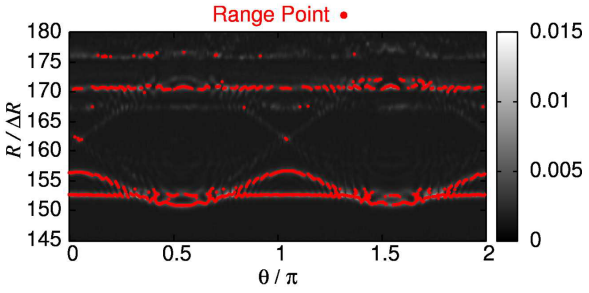

Fig. 23 Output of Capon and extracted range points at the antenna location $(x_1, 0, z_0)$ in the experiment (Case A).

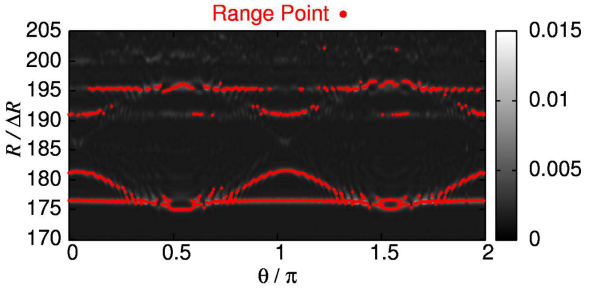

Fig. 24 Output of Capon and extracted range points at the antenna location $(x_2, 0, z_0)$ in the experiment (Case A).

from the front side of the object, the echoes from the target backside, especially for the vertical ring, are weaker, and the range points around the region are sparsely obtained. Moreover, there are significant interferences due to multiple scattering in the region where the two circular rings intersect, and this interference causes slight inaccuracy in range point extraction. Figure 25 shows the 3-D image obtained using the extended RPM method and demonstrates that the estimated boundary reproduces the close 3-D image to the actual boundary, and that the extended RPM method is reasonable for realistic scenes assuming a general solid object. However, there is some image degradation around the crossing points of the two rings because of the resolution degradation of the Capon algorithm due to the multiple scattering interference, and the lower side of the target boundary cannot be obtained because the reflection echoes around the region are abated by obstacles; i.e., the upper side of the target. The mean value of ϵ_i defined in Eq. (16) as $\overline{\epsilon}$ is $2.68\Delta R$ for the conventional method and $0.812\Delta R$ for the extended

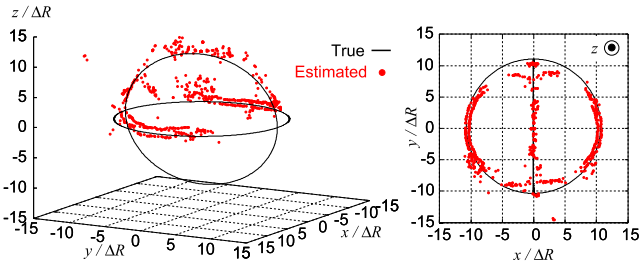

Fig. 25 3-D reconstruction image obtained by the extended RPM method in the experiment (Case A).

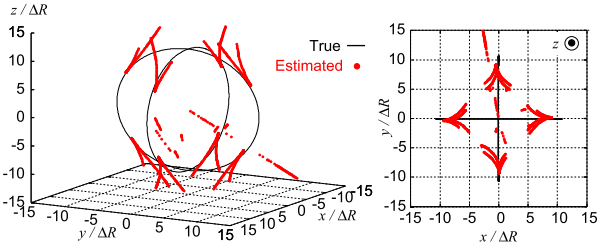

Fig. 26 3-D reconstruction image obtained by the conventional method in the experiment (Case B).

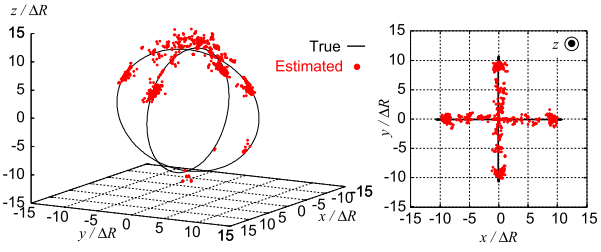

Fig. 27 3-D reconstruction image obtained by the extended RPM method in the experiment (Case B).

RPM method.

To investigate the relevance of the extended RPM method, another target case is investigated, where two annular rings existing $x = 0$ and $y = 0$ planes intersect, and is called "Case B". The antenna locations and the data acquisition parameters are exactly the same as in the previous case. Figures 26 and 27 show the 3-D reconstruction images obtained using the conventional and extended RPM methods, respectively. The mean S/N is around 27 dB in this case. This example verifies that our proposed method correctly produces the outline around the upper side of the actual target boundary, while the conventional method cannot produce a significant image. Note that, as seen in Fig. 27, the interference effects due to multiple scattering between two annular targets degrade the imaging accuracy around the intersection region. $\overline{\epsilon}$ is $2.42\Delta R$ for the conventional method and $0.764\Delta R$ for the extended RPM method, which quantitatively demonstrates that our method has a substantial advantage in the accurate 3-D imaging of objects with continuous boundaries, even in realistic cases. Finally, Fig. 28 shows the number of the estimated target points versus the error

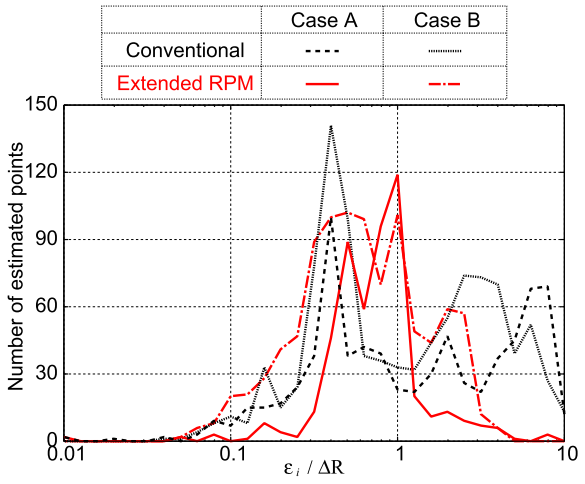

Fig. 28 Histogram of target points with ϵ_i for each target case in the experiment.

ϵ_i, for each target case. This figure quantitatively validates the enhanced accuracy of the extended RPM method compared with that of the conventional method by suppressing the false points with $\epsilon_i \geq 1.0\Delta R$.

6. Conclusion

This paper proposed a novel 3-D reconstruction algorithm by extending the original RPM algorithm to the ISAR model for objects with continuous boundaries, for which the assumption of the conventional ISAR-based method is violated. In this extension, a double mono-static model is introduced to suppress cross-range ambiguity, and two groups of observed ranges are effectively employed to enhance the positioning accuracy for each instantaneous scattering point. The notable advantage of this method is that it is applicable to an object with a continuous boundary, for which a scattering center shifts across the target boundary. It has the additional advantage that the target boundary can be expressed as a group of target points, which enables the identification of an edge or wedge region and helps to classify the target structure. Numerical results confirmed that our method remarkably enhances the accuracy of 3-D target reconstruction, even at lower S/N. In experimental investigations, the proposed method remarkably enhanced the 3-D reconstruction accuracy for two different annular target objects, compared with the accuracy achieved using the conventional ISAR-based method.

References

[1] F. Gini and F. Lombardini, "Multibaseline cross-track SAR interferometry: A signal processing perspective," IEEE Trans. Aerosp. Electron. Syst., vol.20, no.8, pp.71–93, Aug. 2005.
[2] C.V. Jakowatz, Jr. and P.A. Thompson, "A new look at spotlight mode synthetic aperture radar as tomograpgy: Imaging 3-D targets," IEEE Trans. Image Process., vol.4, no.5, pp.699–703, May 1995.
[3] J. Fortuny, "An efficient 3-D near-field ISAR algorithm," IEEE Trans. Aerosp. Electron. Syst., vol.34, no.4, pp.1261–1270, Oct. 1998.
[4] J. Mayhan, M. Burrows, K. Cuomo, and J. Piou, "High resolution 3D snapshot ISAR imaging and feature extraction," IEEE Trans. Aerosp. Electron. Syst., vol.37, no.2, pp.630–642, April 2001.
[5] T. Kempf, M. Peichl, S. Dill, and H. Suess, "3D tower-turntable ISAR imaging," Proc. EuRAD, pp.114–117, Oct. 2007.
[6] X. Xu and R.M. Narayanan, "Three-dimensional interferometric ISAR imaging for target scattering diagnosis and modeling," IEEE Trans. Image Process., vol.10, no.7, pp.1094–1102, July 2001.
[7] G. Wang, X.G. Xia, and V.C. Chen, "Three-dimensional ISAR imaging of maneuvering targets using three receivers," IEEE Trans. Image Process., vol.10, no.3, pp.436–447, March 2001.
[8] C. Ma, T.S. Yeo, Q. Zhang, H.S. Tan, and J. Wang, "Three-dimensional ISAR imaging based on antenna array," IEEE Trans. Geosci. Remote Sens., vol.46, no.2, pp.504–515, Feb. 2008.
[9] M. Iwamoto and T. Kirimoto, "A novel algorithm for reconstructing threedimensional target shapes using sequential radar images," Proc. IEEE IGARSS, vol.4, pp.1607–1609, July 2001.
[10] K. Suwa, K. Yamamoto, M. Iwamoto, and T. Kirimoto, "Reconstruction of 3-D target geometry using radar movie," Proc. EUSAR, pp.149–152, 2008.
[11] E. Ertin, R.L. Moses, and L.C. Potter, "Interferometric methods for three-dimensional target reconstruction with multipass circular SAR," IET Trans. Radar Sonar Navig., vol.4, no.3, pp.463–473, 2010.
[12] Y. Lin, W. Hong, W. Tan, Y. Wang, and Y. Wu, "Interferometric circular SAR method for three-dimensional imaging," IEEE Geosci. Remote Sens. Lett., vol.8, no.6, pp.1026–1030, July 2011.
[13] T. Sakamoto, "A fast algorithm for 3-dimensional imaging with UWB pulse radar systems," IEICE Trans. Commun., vol.E90-B, no.3, pp.636–644, March 2007.
[14] S. Kidera, T. Sakamoto, and T. Sato, "High-resolution and real-time UWB radar imaging algorithm with direct waveform compensations," IEEE Trans. Geosci. Remote Sens., vol.46, no.11, pp.3503–3513, Nov. 2008.
[15] S. Kidera, T. Sakamoto, and T. Sato, "Accurate UWB Radar 3-D imaging algorithm for complex boundary without range points connections," IEEE Trans. Geosci. Remote Sens., vol.48, no.4, pp.1993–2004, April 2010.
[16] S. Kidera, T. Sakamoto, and T. Sato, "Super-resolution UWB radar imaging algorithm based on extended capon with reference signal optimization," IEEE Trans. Antenna Propag., vol.59, no.5, pp.1606–1615, May 2011.
[17] W.G. Carrara, R.S. Goodman, and R.M. Majewski, Spotlight synthetic aperture radar-signal processing algorithm, Artech House, 1995.

Shouhei Kidera received his B.E. degree in Electrical and Electronic Engineering from Kyoto University in 2003 and M.I. and Ph.D. degrees in Informatics from Kyoto University in 2005 and 2007, respectively. He is an assistant professor in Graduate School of Informatics and Engineering, University of Electro-Communications, Japan. His current research interest is in advanced signal processing for the near field radar, UWB radar. He is a member of the Institute of Electrical and Electronics Engineering (IEEE) and the Institute of Electrical Engineering of Japan (IEEJ).

Hiroyuki Yamada received his B.E. and M.E. degrees in Electronic Engineering from University of Electro-Communications in 2009 and 2011, respectively. He joined Software Division, Hitachi Ltd. in 2011.

Tetsuo Kirimoto received the B.S. and M.S. and Ph.D. degrees in Communication Engineering from Osaka University in 1976, 1978 and 1995, respectively. During 1978–2003 he stayed in Mitsubishi Electric Corp. to study radar signal processing. From 1982 to 1983, he stayed as a visiting scientist at the Remote Sensing Laboratory of the University of Kansas. From 2003 to 2007, he joined the University of Kitakyushu as a Professor. Since 2007, he has been with the University of Electro-Communications, where he is a Professor at the Graduate School of Informatics and Engineering. His current study interests include digital signal processing and its application to various sensor systems. Prof. Kirimoto is a member of the Institute of Electrical and Electronics Engineering (IEEE) and and the SICE (Society of Instrument and Control Engineering) of Japan.